Turbulent Fluxes in the Hurricane Boundary Layer. Part I: Momentum Flux

JEFFREY R. FRENCH*

Atmospheric Turbulence and Diffusion Division, NOAA/Air Resources Laboratory, Oak Ridge, Tennessee

WILLIAM M. DRENNAN AND JUN A. ZHANG

Rosenstiel School of Marine and Atmospheric Science, University of Miami, Miami, Florida

PETER G. BLACK

Hurricane Research Division, NOAA/Atlantic Oceanographic and Meteorological Laboratory, Miami, Florida

(Manuscript received 9 March 2006, in final form 20 July 2006)

ABSTRACT

An important outcome from the ONR-sponsored Coupled Boundary Layer Air–Sea Transfer (CBLAST) Hurricane Program is the first-ever direct measurements of momentum flux from within hurricane boundary layers. In 2003, a specially instrumented NOAA P3 aircraft obtained measurements suitable for computing surface wind stress and ultimately estimating drag coefficients in regions with surface wind between 18 and 30 m s^{-1}. Analyses of data are presented from 48 flux legs flown within 400 m of the surface in two storms. Results suggest a roll-off in the drag coefficient at higher wind speeds, in qualitative agreement with laboratory and modeling studies and inferences of drag coefficients using a log-profile method. However, the amount of roll-off and the wind speed at which the roll-off occurs remains uncertain, underscoring the need for additional measurements.

1. Introduction

Heat stored in the warm tropical oceans is the primary source of energy for hurricanes. However, the ocean also removes energy from hurricanes through wind drag on the surface. It has long been realized that even relatively simple conceptual models of tropical cyclones are sensitive to exchange of both heat and momentum between the ocean's surface and the atmosphere (Ooyama 1969; Emanuel 1995). Indeed, Emanuel (1986, 1989, 1995) has continually demonstrated the importance of the ratio of exchange coefficients of enthalpy (C_K) and momentum (drag coefficient; C_D) for maximum storm intensity and for time scales over which tropical cyclones develop. Here C_K is the exchange coefficient of heat and water, assumed to be equal. Emanuel (1995) demonstrates that for hurricanes to attain a maximum wind speed of 50 m s^{-1} or greater, the ratio C_K/C_D must be equal to or greater than 0.75. Further, Emanuel demonstrates that in high wind regions of intense storms the C_K/C_D ratio likely lies within the range of 1.2 to 1.5.

For moderate wind speeds from 5 to 20 m s^{-1} over the ocean, it has been repeatedly shown that the drag coefficient increases nearly monotonically (Smith 1980; Large and Pond 1981; Geernaert et al. 1986; Smith et al. 1992) with wind speed. Additionally, counter swells and fetch- or duration-limited conditions act to further increase drag (Donelan et al. 1997; Drennan et al. 2003), while following swell decreases drag (Drennan et al. 1999). These wave effects account for much of the scatter observed in the existing datasets. However, based on measurements of sensible heat flux (Smith 1980) and both sensible and latent heat flux (DeCosmo et al. 1996) the heat exchange coefficient is independent of wind speed for wind speeds up to 20 m s^{-1}.

* Current affiliation: Department of Atmospheric Sciences, University of Wyoming, Laramie, Wyoming.

Corresponding author address: Dr. Jeffrey R. French, Dept. of Atmospheric Sciences, University of Wyoming, Laramie, WY 82071.
E-mail: jfrench@uwyo.edu

DOI: 10.1175/JAS3887.1

To explicitly model conditions at wind speeds greater than 20 m s^{-1}, including tropical cyclones, requires some sort of extrapolation of the existing flux measurements. The simplest approach, just extending a linear fit to wind speeds greater than 20 m s^{-1}, leads to a decreasing ratio of C_K/C_D and even at wind speeds as low as 20 m s^{-1}, the ratio C_K/C_D is roughly equal to 0.5. This would seem to indicate that it is necessary, at higher wind speeds, for the drag coefficient to decrease and/or that there is a significant increase in the heat exchange coefficient. Indeed, evidence is mounting that the drag coefficient does not continue to increase at higher wind speeds. Modeling studies (i.e., Moon et al. 2004) support a roll-off of the drag coefficient at wind speeds of approximately 35 m s^{-1} due to wave effects. Donelan et al. (2004) provided the first direct measurements from Laboratory wave-tank studies. Their results indicate a saturation or roll-off of the drag coefficient to a near-constant value at wind speeds greater than 33 m s^{-1}. Powell et al. (2003) found similar results from inferred drag coefficients from 331 GPS sonde wind profiles in 15 tropical cyclones. Assuming a mean log profile, the Powell et al. results indicate a leveling off and even a decrease of the drag coefficient somewhere between 30 and 35 m s^{-1}. However, even above the roll-off limit of Donelan et al. and Powell et al., the C_K/C_D ratio remains around one-half. Therefore, despite these recent breakthroughs and due in large part to the difficulty in obtaining the necessary measurements in high wind boundary layers, there remains a great deal of uncertainty in regards to the relationship between exchange coefficients and wind speed in high wind conditions.

A primary objective of the Coupled Boundary Layer Air–Sea Transfer (CBLAST) Hurricane program is to obtain measurements suitable for the computation of near-surface fluxes of heat and momentum in hurricanes. Black et al. (2007) present an overview of the CBLAST Hurricane program including details on experiments, assets, and objectives. The work presented herein focuses on measurements of the near-surface fluxes of momentum obtained from an instrumented aircraft. Section 2 discusses measurements from the aircraft. Here we outline the computation of the three-dimensional wind vector from two similar instruments on the same aircraft. In section 3 we present our analysis methods including data quality assurance and the computation of surface momentum fluxes. Our results are presented in section 4. Section 5 provides some concluding remarks. A similar analysis of measurements pertaining to fluxes of latent heat is presented in a companion paper (Drennan et al. 2007).

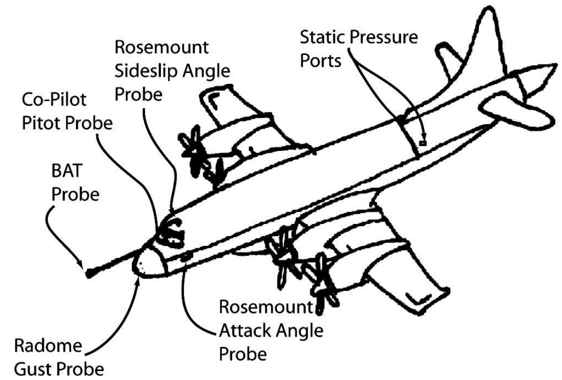

FIG. 1. Sketch of the NOAA P3 research aircraft (N43RF) showing the location of instrumentation relevant to this study.

2. Measurements

A specially instrumented National Oceanic and Atmospheric Administration (NOAA) WP-3D Orion aircraft (hereafter referred to by its call sign, N43RF) was used to obtain boundary layer measurements suitable for the computation of heat and momentum flux. Because the hurricane environment makes it difficult to obtain measurements with an aircraft very near the surface, a flight strategy was developed to utilize a series of straight and level flux runs beginning near the top of the boundary layer with successively lower-altitude legs until a final leg of roughly 60 to 100 m altitude was completed. Such a stepped descent series of runs may include as many as five flux legs of roughly 15 to 55 km in length. Ideally, a full stepped descent pattern consists of a series of legs oriented parallel to the mean flight-level wind vector and a second series of legs oriented perpendicular to the mean flight-level wind vector.

Safety requirements dictate all boundary layer legs are to be flown in rain-free conditions. A typical flight pattern then consists of a survey pattern (i.e., a figure four through the storm typically between 1.5 and 3 km altitude) followed by one or two full stepped descents in a suitably identified region of the storm. Primary considerations for suitability include space available between rainbands for completing flux legs and location within storm with regard both to distance from the center and storm quadrant. The interested reader is referred to Black et al. (2007) for more detailed discussion of the flight patterns and considerations.

a. N43RF instrumentation

For the CBLAST Hurricane experiment, N43RF was instrumented with three independent systems for measuring aircraft-relative air velocity (Fig. 1): a five-hole nose radome system (Brown et al. 1983; Khelif et al.

1999), a system consisting of two Rosemount 858Y probes and a pitot tube, and an NOAA/Air Resources Laboratory (ARL) designed nine-hole gust probe system (Crawford and Dobosy 1992; Hacker and Crawford 1999). From data obtained during calibration maneuvers performed in advance of the 2003 measurement campaign, it is noted that one of the pressure ports from the nose radome system leaked. Further, examination of data from flux runs conducted after penetrations of regions of heavy rain indicate water intrusion into one or more of the radome ports was common. Thus, for the remainder of the analysis, data will be presented only from the Rosemount system and the ARL nine-hole probe.

1) ROSEMOUNT SYSTEM

The standard system for computing the three-dimensional wind vector from N43RF consists of two Rosemount 858Y probes mounted on the aircraft fuselage, one above and behind the cockpit to provide a measurement suitable for the computation of sideslip angle, β, and a second mounted on the pilot side of the fuselage to provide a measurement suitable for computing attack angle, α. A pitot tube mounted on the copilot side of fuselage provides a measure of dynamic pressure. Static pressure is measured from the standard aircraft fuselage static ports. Static pressure from the fuselage port is corrected by +0.3 hPa following Khelif et al. (1999).

Analog data from the Rosemount system are first filtered to reduce aliasing and then digitized at 40 Hz. The data are ingested by the standard aircraft data system. GPS time tags are provided for synchronizing these data with data from other systems on the aircraft.

2) BAT SYSTEM

An ARL nine-hole probe (BAT for Best Aircraft Turbulence and because it is shaped like a baseball bat) was installed on N43RF prior to the 2002 hurricane season. It differs from the Rosemount and other gust probe systems by utilizing measurements from nine pressure ports to provide direct measurements of three differential pressures and a reference pressure that, when adjusted for flow angles, provides a measure of the static pressure. In addition, the BAT installation contains a GPS sensor and three-plane orthogonal accelerometers. The GPS and accelerometer measurements are combined in post processing to provide a measure of the ground-relative velocity of the probe. The analog signals from the BAT are antialias filtered with a cutoff of 32 Hz, digitally sampled at 1.6 kHz, box-car averaged to 50 Hz (32 oversamples) and recorded by a Linux-based data system. All of the data are GPS time tagged to allow for synchronization with data from the main P3 data system postflight.

The standard BAT probe was originally designed for boundary layer measurements in benign environments from slow flying single-engine aircraft. The earliest version of hurricane BAT probe, test flown in 2002, was modified from the standard BAT probe by utilizing a pump system to back-flush air through the pressure ports. This eliminates contamination due to water infiltration into the ports in heavy rain. During measurement periods, the pumps are turned off. Following flights into storms in 2002 and early 2003, further modifications were made. These include an addition of a drain hole for the center port and a machined aluminum hemisphere and mount ring. The more rugged structure eliminates damage to the probe due to impact of hydrometeors at P3 flight speeds (French et al. 2004).

b. *Wind computation*

The three-dimensional wind vector is computed by taking the vector sum of the aircraft-relative air velocity and the ground-relative aircraft velocity. The aircraft-relative air velocity is determined independently from the two gust probe systems and is rotated into the earth coordinate system using a transformation matrix, $\mathbf{T}$, defined by the aircraft attitude:

$$\mathbf{V}_{\text{air}} = [\mathbf{T}] \cdot \mathbf{V}'_{\text{air}}, \tag{1}$$

where the prime indicates the aircraft coordinate system. For both gust probe systems, the aircraft attitude is provided by the onboard inertial navigation system (INS).

Both gust probe systems provide measures of differential and absolute pressures from which angles of attack (α), sideslip (β), dynamic (Q), and static pressures (P_s) are determined as described in the following section. Given Q, α, β, and P_s, and utilizing moist thermodynamics the aircraft-relative air velocity vector is computed. For this computation, the temperature is taken from a sensor on the BAT and the dewpoint is from a General Eastern model 1011 chilled mirror.

The INS provides the ground-relative velocity for the Rosemount system. The translation velocity from the INS is measured in earth coordinates and thus does not need to be rotated. Added to this is the resultant velocity due to platform rotation and spatial displacement between the gust probes and the INS. For the Rosemount system the ground velocity is given by

$$\mathbf{V}_{\text{gnd}} = \mathbf{V}_{\text{ins}} + [\mathbf{T}] \cdot (\mathbf{\Omega}' \cdot \mathbf{L}), \tag{2}$$

where $\mathbf{\Omega}'$ is the rotation rate of the aircraft about the INS and $\mathbf{L}$ is the vector displacement between the gust probe and the INS.

For the BAT system, the ground-relative velocity is measured on the probe. Measurements from probe accelerometers are rotated to earth coordinates using the transformation matrix, $\mathbf{T}$, and then integrated to compute earth-relative velocity. Measurements from the integrated accelerometers and from the BAT GPS are combined using an FFT complimentary filtering technique with blending frequencies from 1/4 to 4/9 Hz. Frequencies lower than 1/4 Hz are provided by GPS, higher than 4/9 Hz are provided by integrated accelerometer measurements.

c. System dynamic calibration

Dynamic calibration and systems performance tests are conducted by evaluating the computed wind vector during certain prescribed flight maneuvers. In the most general terms, maneuvers of the type described by Brown et al. (1983), Lenschow (1986), and Tjernström and Friehe (1991), are performed in quiescent air. For a given maneuver, each component of the computed wind vector is evaluated in terms of both the mean value and variance. An iterative method is used to obtain convergence of the calibration coefficients by minimizing correlations between the computed wind vector and pilot induced aircraft motions.

Both gust probe systems provide measures of differential attack pressure, P_α, and differential sideslip pressure, P_β. These measurements respond to departures from zero of angle of attack (P_α) and angle of sideslip (P_β). Additionally the BAT provides a measure of the differential impact pressure (P_x) that is the measured pneumatic pressure difference between the center hole on the BAT and four reference ports; P_x is closely related to the dynamic pressure, Q. The reference pressure, P_r, from the BAT is the pneumatic average from four ports and is used to determine the static pressure.

A basic solution to the wind triangle begins with determining the aircraft-relative air velocity, found by computing the flow angles and the dynamic and static pressures. The angle of attack in radians from the BAT is first estimated using the measurements P_α and P_x:

$$\alpha' \cong \varepsilon_\alpha k_\alpha \frac{P_\alpha}{P_x}, \tag{3}$$

where k_α is the probe sensitivity and is equal to 2/9 given the geometry of the probe and location of the holes. The error of k_α, denoted ε_α, is introduced as a calibration factor of the system. Refining the solutions for attack angle, beginning with the National Center for Atmospheric Research (NCAR) method developed by Brown et al. (1983) and further modified for the BAT probe geometry by R. Eckman (1999, unpublished NOAA technical note), we are left with an exact solution for α:

$$\alpha = \operatorname{atan}\left[\frac{(2\alpha')}{1 + \sqrt{1 + 2(\alpha'^2 + \beta'^2)}}\right]. \tag{4}$$

A similar relationship can be used to determine the sideslip angle for the BAT from k_β, P_β, P_x, and ε_β. By substituting Q for P_x in (3), Eqs. (3) and (4) are also valid for the geometry of Rosemount probe and are used to determine α and β from the Rosemount measurements.

The reference pressure is related to the static pressure by

$$P_s = P_r + 0.75Q\left[\frac{\tan^2\alpha + \tan^2\beta}{1 + \tan^2\alpha + \tan^2\beta}\right], \tag{5}$$

where the dynamic pressure is computed from

$$Q = 2.0\,\mathrm{err}Q\,P_x\left[\frac{1 + \tan^2\alpha + \tan^2\beta}{2 - \tan^2\alpha - \tan^2\beta}\right]. \tag{6}$$

From (5) it is apparent that the static pressure is equal to the reference pressure in the absence of motion (zero Q) or for zero attack and sideslip angles. Similarly, from (6), the dynamic pressure, Q, is simply equal to P_x for zero attack and sideslip angles. However, an additional calibration factor, err$Q$, is added in (6) and allows adjustments to the computed dynamic pressure. Here err$Q$ is determined through in-flight maneuvers by forcing the difference of the mean horizontal wind computed from opposing flight legs (into and out of the wind) to zero. Typical values for err$Q$ on the P3 BAT installation are between 1.05 and 1.08 and are primarily accounted for owing to pressure loss through drain holes in the center port. For the Rosemount, Q and P_s are measured independently of the probe. Processing of the Rosemount data also allows for an err$Q$, similar to the BAT data processing.

The vertical component of the aircraft-relative air velocity is corrected for upwash following a treatment similar to Crawford et al. (1996). The upwash factor is determined empirically by forcing the mean computed vertical wind to zero over a range of airspeeds and attack angles for straight and level flight.

Attack angle maneuvers are designed to vary the angle of attack while minimizing variation in airspeed and maintaining little or no sideslip. In doing this, variations in the computed vertical wind can be minimized through an appropriate choice of value for ε_α. Figure 2

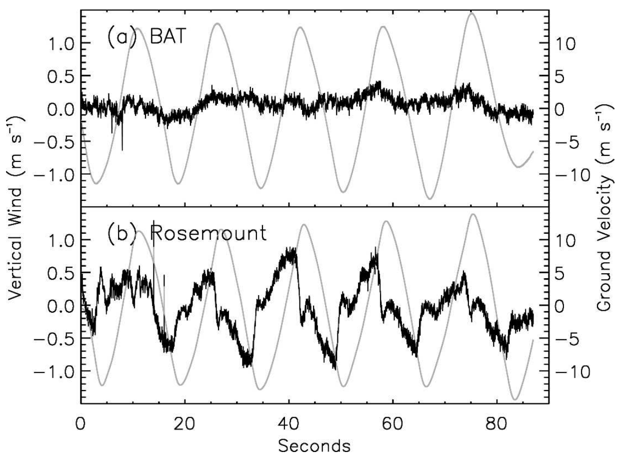

FIG. 2. Vertical wind (black) and ground-relative vertical aircraft velocity (gray) computed from the (a) BAT probe and (b) Rosemount probe during angle of attack (pitching) maneuvers. The scale for the vertical wind (left) is 10% of the scale of the ground-relative vertical aircraft velocity (right).

shows the vertical wind computed during pitching maneuvers in a calibration flight prior to hurricane research flights in 2003. The maneuvers were conducted over the Gulf of Mexico at an altitude of 950 m in clear, nondisturbed air. Determined during straight and level flight, before and after the pitching maneuvers, real variance in the vertical wind is roughly 0.2 m s^{-1}. The general rule of thumb criterion for acceptable calibration of the system is that peak-to-peak variation in the vertical wind should be less than 10% the variation of the ground-relative aircraft velocity. Note that for the BAT variation in the vertical wind is roughly 2% and for the Rosemount variation is roughly 8% of the ground-relative aircraft velocity.

In the absence of any real variation in the vertical wind, changes in attack angle are due solely to pilot input. Consequently, miscalibration of the system leads to variation in computed vertical wind that is correlated with attack angle. Figure 3 shows vertical wind as a function of attack angle for the same time period in Fig. 2. For the BAT, there is virtually no correlation between the two leading to the conclusion that the variation in the computed vertical wind during this period is due primarily to real atmospheric fluctuations. However, the computed vertical wind for the Rosemount probe shows two inflection points, one at 0° and another at 2°. Data lying outside of this range of attack angle appear corrupted, likely due to flow distortion effects from instruments upstream of the Rosemount Probe mounted on the side of the fuselage. However, even in the highly turbulent hurricane boundary layer, rarely does the attack angle fall outside of these bounds. Figure 4 shows the vertical velocity from both probes for a two-minute segment during a flux run in Hurricane Isabel. The measurements are remarkably similar. In Fig. 4b, the data are shown for a 10-s segment of the same run. The only notable difference is the high frequency variations from the BAT measurements that are not evident in the Rosemount measurements due to slower instrument response.

Evaluation of the computation of horizontal winds is accomplished by comparing the mean wind vector for four legs from a box pattern. Evaluations of this type were done for data collected near the beginning of every flight. The box pattern was typically flown at an altitude of 1500 m with 1–2-min legs per side. Figure 5 shows results from six research flights in 2003. In general, the mean wind for a given leg is within 1 to 2 m s^{-1} of the mean from the other legs. An exception is on 3 September when there appears significant variation (4 m s^{-1}) in legs due to a real spatial variation in the wind.

3. Momentum fluxes

The flux data presented herein are from measurements made during six flights in two storms in 2003. The

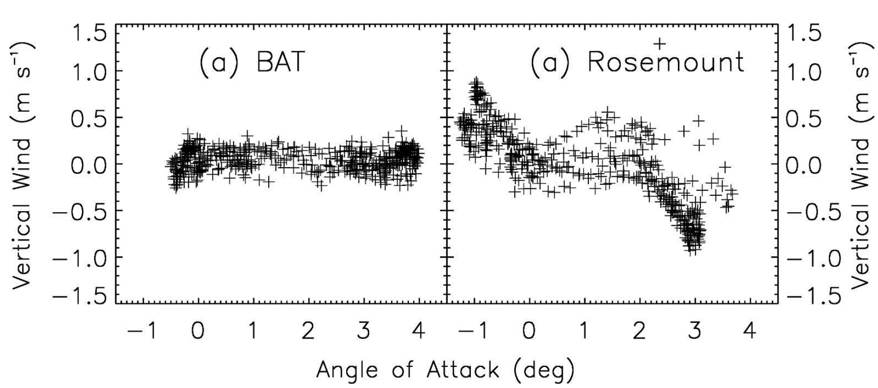

FIG. 3. Vertical wind as a function of attack angle for the (a) BAT probe and (b) Rosemount probe. Data are from the same time period shown in Fig. 2.

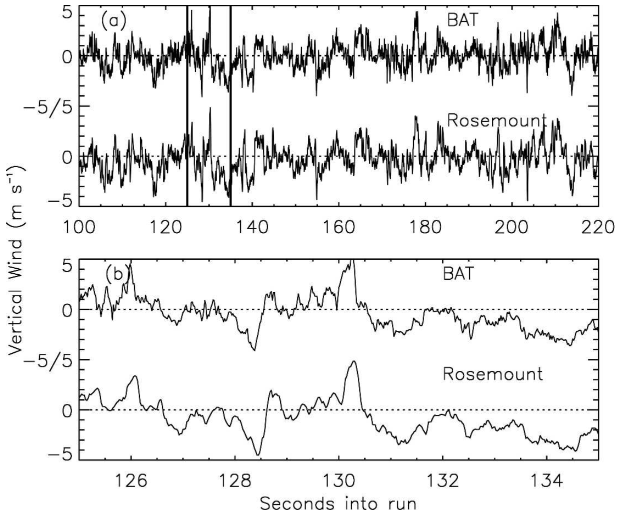

FIG. 4. Vertical wind from the BAT and Rosemount for a 120-s segment (a) of flux run 3 on 14 September. (b) The vertical bars indicate the 10-s time period.

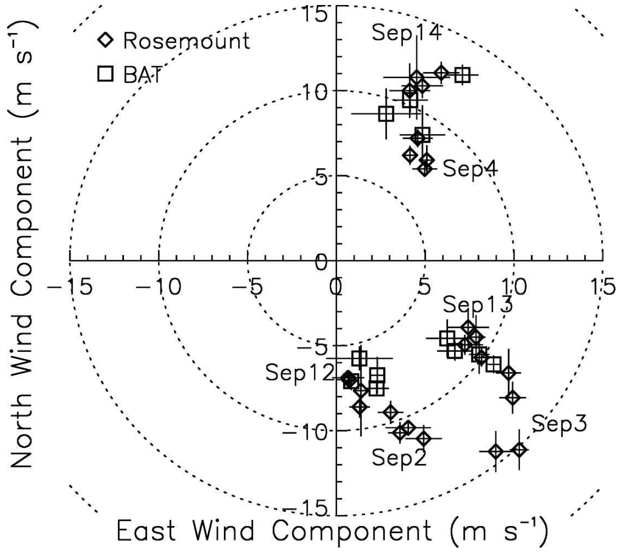

FIG. 5. Mean wind vector (and standard deviation) from individual legs for box patterns flown near the beginning of the six hurricane research flights. Diamonds are for calculations from the Rosemount (all six days) and squares are for calculations from the BAT (last three days).

flights occurred on 2, 3, and 4 September into Hurricane Fabian and 12, 13, and 14 September into Hurricane Isabel. During all six flights the hurricanes were either category 4 or 5. Details of the flight patterns related to storm position and movement of the storms are discussed in Black et al. (2007) and Drennan et al. (2007).

Data presented from Hurricane Fabian are derived from the Rosemount system (the BAT was inoperable during these flights). Data from Hurricane Isabel are derived from the BAT system. To assure continuity of measurements between probes, and hence storms, comparisons are shown in Fig. 6 for the covariance from Rosemount measurements and from BAT measurements for flux runs in Hurricane Isabel. The correlation between the two datasets is 0.75 and is reasonable given the noisy nature of the calculation.

A total of 59 flux runs from altitudes below 400 m were completed in the two storms. Measurements from dropsondes in both storms suggest that the top of the boundary layer at the locations of the flux runs was near 500 m (Drennan et al. 2007). Wind, temperature, and humidity data from these flux runs are used to compute wind stress, friction velocity, and ultimately estimate the 10-m neutral drag coefficient. Beginning and ending times for a given run are chosen initially based on markers set in-flight and are modified in post-flight analysis to remove sections where the aircraft is not straight and level or the plane passes through rain at the beginning or end of the leg leading to spikes in the wind data.

Data quality assurance for individual flux legs include inspection of the linear cumulative summation of the covariance, the power spectra for individual wind components, and cospectra and ogives (Friehe et al. 1991) for along-wind and crosswind stress. Eleven runs are discarded based on this analysis. Figure 7 shows six panels: two each containing graphs from two flux runs for linear cumulative summation of along-wind covariance (Figs. 7a and 7b), along-wind cospectra (Figs. 7c and 7d), and ogives for along-wind covariance (Figs. 7e and 7f). Data from two discarded runs are shown on the left panels. The right panels show data from two good runs. For the discarded runs, disturbances over

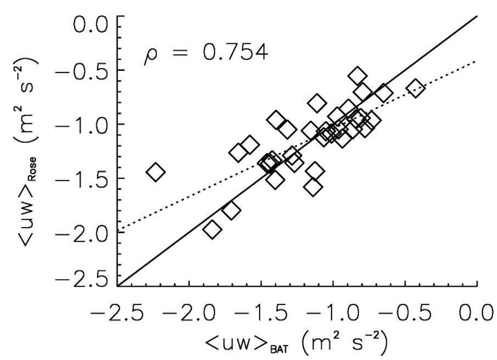

FIG. 6. Scatter diagram of the along-wind covariance from the Rosemount probe and the BAT probe from all flux runs during which both probes were operable. The solid line represents a 1:1 correspondence and the dashed line shows the best fit. The correlation coefficient for these data is $\rho = 0.754$.

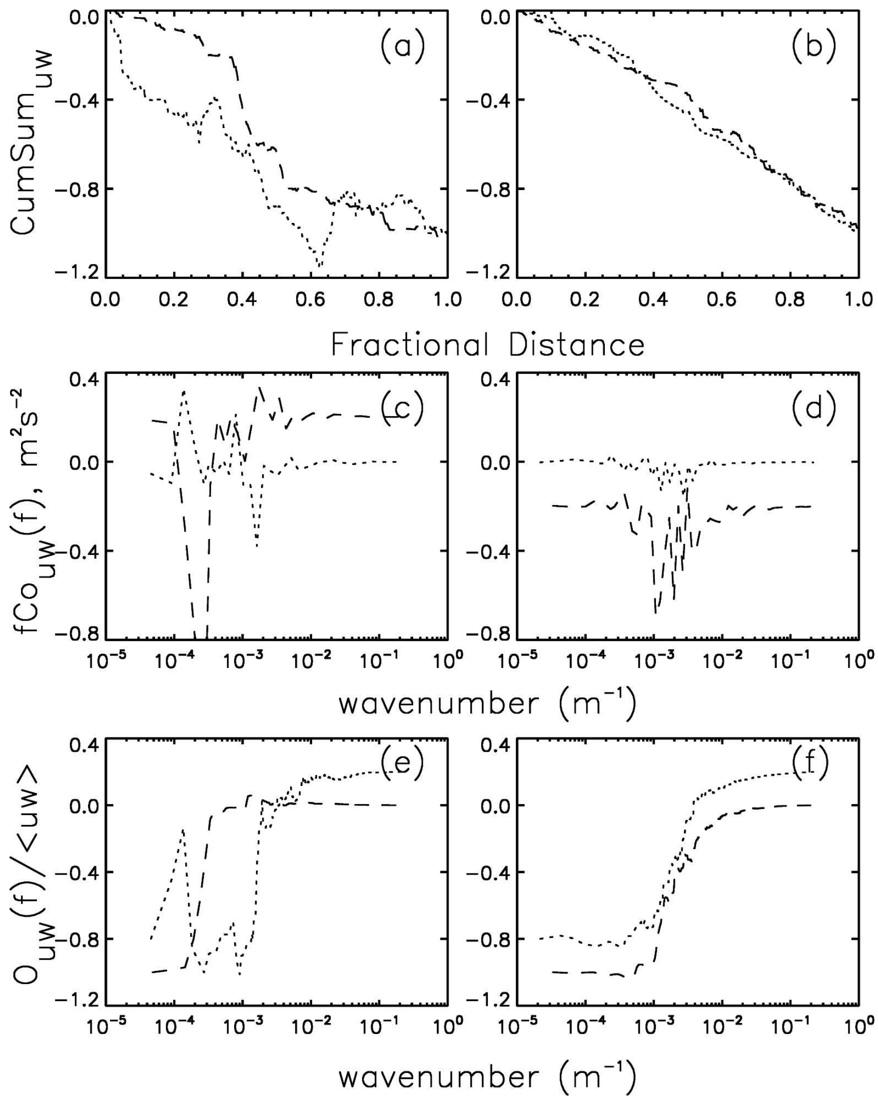

FIG. 7. Data are shown from (left) two discarded runs and (right) two good runs. (a), (b) The top two graphs show the cumulative summation of the along-wind covariance plotted as the fractional distance along the flux run. Here the cumulative summation is normalized by the total covariance. (c), (d) The middle two graphs show frequency-weighted cospectra as a function of wavenumber. To aid in comparison one of the lines in each graph is offset by 0.2 m^2 s^{-2}. (e), (f) The bottom two graphs show ogives (normalized by total covariance). The summation begins at the right (largest wavenumber) and proceeds to the left (smallest wavenumber, largest spatial scales).

small portions of the run affect the total wind stress by as much as 20%–30%. This is reflected in the cumulative sum as sharp changes over small distances. Note that the cospectra and ogives do not appear "well behaved" for these runs. It is possible that organized mesoscale features such as boundary layer rolls are responsible (Foster 2005), but that is only conjecture at this point. For the analysis presented herein, data from discarded runs are excluded but do warrant further investigation.

For the accepted runs, the linear cumulative summation remains with a near constant slope over the entire run. Both the cospectra and the ogives reveal consistent behavior between runs and suggest that the majority of the energy in the momentum flux is from eddies ranging from 100 m to 3 km in size.

Table 1 summarizes the measurements and calculations for each of the 48 runs suitable for this analysis. The majority of the runs (34 out of 48) are oriented along the mean wind vector, reflecting the difficulty in

TABLE 1. Summary of data and calculations from 12 stepped descents (48 flux runs) in three storms for this study.

Date (Sep)	Run	Type	Leg length (km)	Alt (m)	P (mb)	Flight level Wind (m s^{-1})	Flight level Temperature (°C)	SST (°C)	U_{10N} (m s^{-1})	$\langle u'w' \rangle$ (m^2 s^{-2})	$\langle v'w' \rangle$ (m^2 s^{-2})	u_* (m s^{-1})	$C_{D,10N}$ ($\times 10^3$)	Q_{10N} (g kg^{-1})	Q_0 (g kg^{-1})	$\langle q'w' \rangle$ (g kg^{-1} m^1 s^{-1})	q_* (g kg^{-1})	$C_{E,10N}$ ($\times 10^3$)
2	1	Along	49.5	278	969.9	32.6	23.9	26.7	22.9	−0.73	−0.32	0.99	1.84	17.77	22.58	0.14	−0.14	1.25
	2	Along	30.6	179	981.6	29.7	24.7	26.7	21.8	−0.52	−0.25	0.82	1.40	17.74	22.28	0.13	−0.15	1.30
	3	Along	46.0	136	987.5	28.3	24.8	26.6	21.3	−0.78	−0.23	0.95	1.98	17.56	21.98	0.12	−0.12	1.28
	4	Along	26.0	79	991.7	29.1	25.7	26.7	24.8	−0.56	−0.18	0.80	1.02	17.72	22.04	0.08	−0.10	0.77
	5	Cross	29.9	288	969.8	33.4	24.2	26.8	24.2	−0.37	−0.27	0.77	1.00	17.97	22.69	0.15	−0.19	1.29
3	1	Along	27.6	376	959.7	32.2	23.0	30.0	24.7	−0.86	−0.68	1.17	2.22	18.49	27.77	0.19	−0.16	0.81
	2	Along	20.7	278	970.2	40.5	22.4	29.8	29.0	−0.74	−0.30	0.98	1.14	15.27	27.11	0.35	−0.34	1.01
	3	Along	27.4	187	979.2	37.2	23.5	29.7	28.7	−1.90	−0.01	1.44	2.51	15.83	26.62	0.51	−0.34	1.64
	4	Along	29.9	196	979.4	34.9	23.7	29.9	28.1	−1.26	0.05	1.19	1.79	15.69	26.94	0.34	−0.27	1.07
	5	Along	32.2	132	985.6	30.7	24.9	29.8	26.6	−1.02	0.18	1.06	1.59	15.29	26.73	0.23	−0.21	0.75
	6	Cross	33.4	270	970.1	36.4	25.1	29.3	28.9	−0.89	0.16	1.04	1.29	14.78	26.30	0.23	−0.21	0.69
	7	Cross	26.5	157	982.9	35.9	25.3	29.2	28.1	−1.43	0.01	1.25	1.97	14.82	25.86	0.31	−0.25	0.99
4	1	Along	28.8	368	964.8	30.3	24.2	29.1	21.9	−0.24	−0.13	0.64	0.82	—	—	—	—	—
	2	Along	32.2	364	964.9	30.4	24.3	29.2	22.6	−0.41	−0.37	0.86	1.43	—	—	—	—	—
	3	Along	25.3	369	965.3	29.9	24.5	29.0	21.4	−0.33	−0.31	0.80	1.36	18.30	25.94	0.18	−0.21	1.09
	4	Along	20.5	280	974.8	28.4	24.6	29.7	20.2	−0.48	−0.08	0.79	1.51	—	—	—	—	—
	5	Along	20.7	194	984.1	26.7	25.7	29.8	20.8	−1.08	0.04	1.11	2.81	17.86	26.74	0.16	−0.14	0.86
	6	Along	26.5	135	990.6	22.2	25.7	29.7	18.7	−0.48	−0.20	0.76	1.67	17.41	26.43	0.09	−0.12	0.55
	7	Along	14.0	104	992.7	21.5	25.3	29.5	22.0	−0.46	−0.01	0.71	1.05	17.98	26.09	0.08	−0.11	0.44
12	1	Along	63.3	374	962.6	35.2	25.0	26.2	24.5	−0.52	−0.49	0.97	1.54	19.98	22.18	0.14	−0.14	2.53
	2	Along	26.5	286	973.3	32.2	25.9	26.2	18.9	−0.22	−0.21	0.64	1.13	19.78	21.95	0.10	−0.15	2.44
	3	Along	54.1	194	982.1	31.4	26.5	26.4	19.1	−0.58	−0.26	0.86	2.03	19.24	21.98	0.08	−0.08	1.46
	4	Along	26.8	137	989.4	25.2	26.9	26.2	16.5	−0.57	−0.08	0.81	2.38	19.13	21.47	0.07	−0.08	1.71
	5	Along	31.1	88	994.8	24.3	27.4	27.4	20.3	−0.62	−0.24	0.85	1.74	19.02	23.00	0.10	−0.12	1.24
	6	Cross	29.9	126	987.1	32.6	27.0	27.6	24.5	−1.23	−1.01	1.30	2.83	18.80	23.52	0.06	−0.04	0.49
	7	Cross	32.2	95	992.8	26.9	27.3	27.8	22.0	−0.68	−0.26	0.89	1.62	19.04	23.61	0.09	−0.10	0.93
	8	Cross	25.3	191	981.4	31.3	26.5	27.7	21.6	−0.75	−0.82	1.12	2.69	—	—	—	—	—
	9	Cross	34.5	279	973.1	29.9	25.8	27.8	21.6	−0.36	−0.43	0.85	1.51	18.74	24.17	0.10	−0.11	0.83
13	1	Along	46.0	365	960.8	35.6	25.4	26.7	19.8	−0.36	−0.37	0.84	1.77	20.08	22.81	0.08	−0.10	1.56
	2	Along	24.2	256	972.1	35.3	26.4	26.8	21.9	−0.28	−0.86	1.04	2.21	19.90	22.72	0.12	−0.11	1.88
	3	Along	46.0	189	980.8	33.0	26.9	26.8	19.7	−0.64	−0.33	0.91	2.12	19.64	22.45	0.05	−0.05	0.93
	4	Along	28.8	120	988.2	29.5	27.6	26.7	21.2	−0.71	−0.10	0.89	1.74	19.66	22.16	0.08	−0.08	1.45
	5	Along	25.3	70	992.6	27.8	27.7	26.7	24.7	−0.85	−0.11	0.95	1.48	19.45	22.05	0.07	−0.07	1.12
	6	Cross	32.2	269	972.1	36.3	26.1	27.4	24.0	−0.77	−0.89	1.18	1.47	—	—	—	—	—
	7	Cross	34.5	193	981.3	31.1	26.7	27.4	22.6	−0.59	−0.48	0.94	1.72	19.23	23.25	0.11	−0.12	1.22

TABLE 1. (*Continued*)

Date (Sep)	Run	Type	Leg length (km)	Alt (m)	P (mb)	Flight level Wind (m s^{-1})	Flight level Temperature (°C)	SST (°C)	U_{10N} (m s^{-1})	$\langle u'w' \rangle$ (m^2 s^{-2})	$\langle v'w' \rangle$ (m^2 s^{-2})	u_* (m s^{-1})	$C_{D,10N}$ ($\times 10^3$)	Q_{10N} (g kg^{-1})	Q_0 (g kg^{-1})	$\langle q'w' \rangle$ (g kg^{-1} m^1 s^{-1})	q_* (g kg^{-1})	$C_{E,10N}$ ($\times 10^3$)
14	1	Along	46.0	278	971.8	34.8	26.9	28.7	22.9	−0.56	−0.49	0.97	1.76	19.19	25.46	0.12	−0.12	0.82
	2	Along	29.9	179	982.0	29.5	27.8	28.7	22.5	−0.67	−0.22	0.91	1.62	19.64	25.23	0.18	−0.20	1.45
	3	Along	46.0	132	986.1	31.4	28.2	28.7	23.3	−1.01	−0.41	1.10	2.15	19.32	25.10	0.16	−0.14	1.18
	4	Along	13.8	94	990.4	32.0	28.4	28.6	25.7	−1.01	−0.45	1.09	1.79	19.26	24.84	0.14	−0.12	0.95
	5	Along	16.1	104	988.0	31.0	28.3	28.6	27.6	−1.22	−0.07	1.14	1.71	19.54	24.91	0.21	−0.18	1.44
	6	Cross	38.0	383	960.3	30.2	26.0	28.8	22.2	−0.63	−0.81	1.16	2.66	19.34	25.95	0.18	−0.15	1.23
	7	Cross	23.0	268	973.3	32.9	27.1	28.9	21.6	−0.72	−0.60	1.07	2.41	19.35	25.65	0.17	−0.15	1.25
	8	Cross	38.0	187	982.2	27.2	27.6	28.9	20.9	−0.71	−0.44	0.99	2.22	19.67	25.38	0.17	−0.17	1.41
	9	Cross	25.3	120	989.7	29.1	28.4	28.9	22.4	−0.82	−0.57	1.05	2.18	19.16	25.19	0.10	−0.09	0.75
	10	Cross	26.5	76	996.1	22.7	28.7	28.8	24.2	−0.81	−0.30	0.96	1.56	19.45	25.02	0.13	−0.14	0.98
	11	Along	23.0	361	956.3	36.4	25.4	29.0	24.6	−0.44	−0.69	1.04	1.75	18.90	26.37	0.16	−0.15	0.89
	12	Along	28.8	277	966.1	31.7	26.9	29.3	23.9	−0.76	−0.51	1.06	1.94	19.56	26.45	0.28	−0.26	1.72
	13	Along	15.0	185	975.6	34.1	27.5	29.0	22.5	−1.12	−0.58	1.20	2.81	—	—	—	—	—

finding a long enough path of rain-free space in the crosswind direction. The average air-relative leg length is roughly 28 km, with a minimum of 13 km from one of the lower altitude legs and a maximum of more than 55 km. The majority of legs are between 20 and 30 km in length. The lowest altitude leg is 70 m. Only six legs are at altitudes less than 100 m.

Leg-averaged mean flight level winds speeds vary from 21 m s^{-1} to just over 40 m s^{-1}, with most between 30 and 35 m s^{-1}. The near-surface neutral-stability wind speed, $U_{10\text{N}}$, is taken from the nadir-pointing stepped frequency microwave radiometer (SFMR). Details comparing several approaches for estimating U_{10N} in this study are presented in the companion paper Drennan et al. (2007). Here, we summarize by saying that the SFMR was originally calibrated against roughly 250 collocated samples from GPS dropsondes for computing 1-min-averaged U_{10N} (Uhlhorn and Black 2003). Results in this study use the latest SFMR wind speed algorithm, SWEMODv2 based on data from the 2005 hurricane season (Uhlhorn et al. 2007). Values of U_{10N} vary from a minimum of roughly 17 m s^{-1} to a maximum of 29 m s^{-1}.

The covariance is computed by rotating the wind vector into its along-wind and crosswind components followed by removing the mean over the entire leg. The magnitude of the momentum flux may then be calculated:

$$|\boldsymbol{\tau}| = -\rho[\overline{u'w'}^2 + \overline{v'w'}^2]^{1/2}, \tag{7}$$

where ρ is the air density and $\overline{u'w'}$ and $\overline{v'w'}$ are the along-wind and crosswind components of the covariance (columns 9 and 10, Table 1) for a given flux leg. In this analysis we do not assume a constant wind direction throughout an entire leg. Thus, the reader is cautioned that the magnitude of the along- and crosswind components of the covariance is highly dependant on the amount of turning of the wind and how changes in wind direction and magnitude over the course of a single run are interpreted in the analysis (i.e., how variations in the horizontal wind vector are broken into variations in the along-wind component and the crosswind component). However, the total covariance and hence the stress is unaffected.

Figure 8 illustrates variation in $|\tau/\rho|^{1/2}$ with altitude. Data from each stepped descent in this study are shown in separate panels. An initial approach of estimating the surface value (friction velocity, $u_* = |\tau/\rho|_{\text{sfc}}^{1/2}$) based on linear regression and extrapolating to the surface results in the dashed lines shown in the figure. This method works reasonably well for stepped descents that consist of several flux legs at different altitudes.

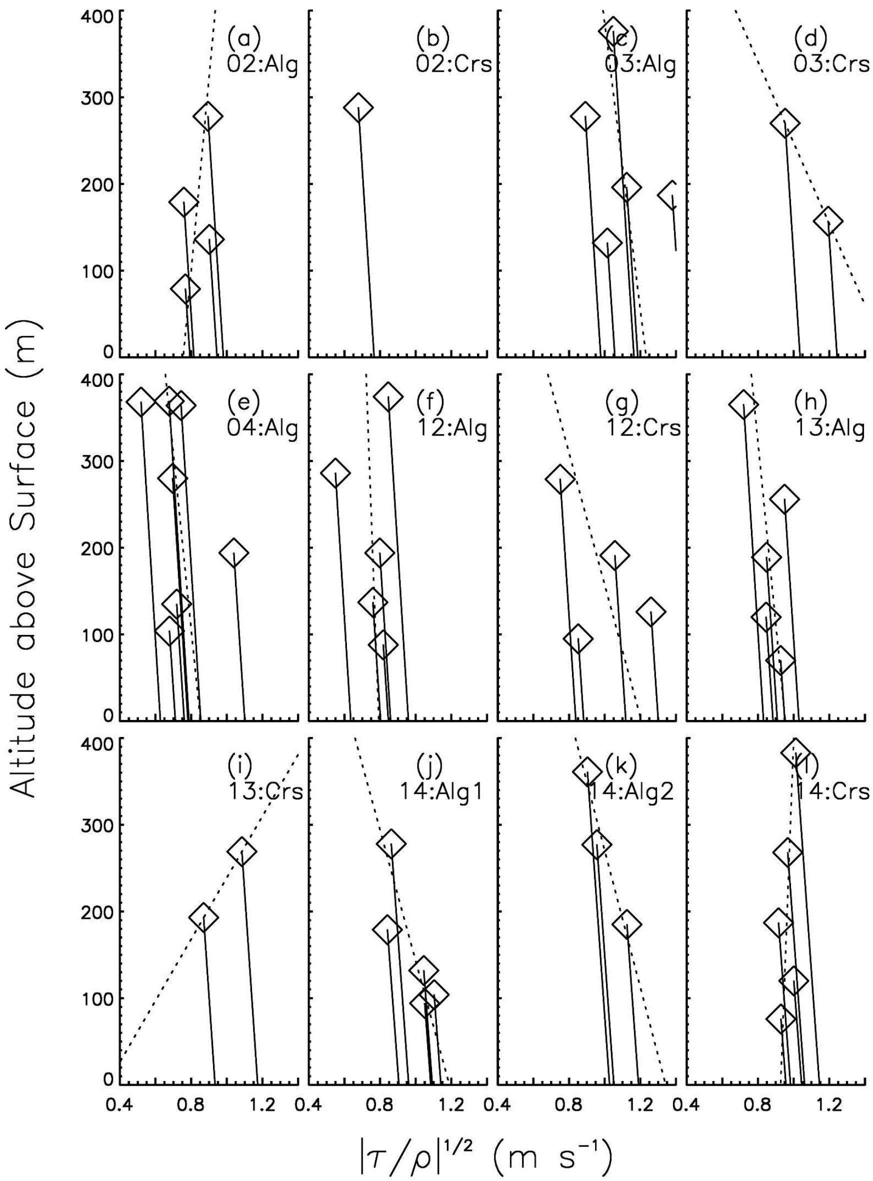

FIG. 8. Total covariance ($|\tau/\rho|^{1/2}$) as a function of altitude for 12 individual stepped descents. The dashed line shows the best linear fit, extrapolated to the surface. The solid lines show the extrapolation of friction velocity following Donelan (1990; see text). Crs and Alg designators represent crosswind and along-wind runs, respectively.

Many of the stepped descents, crosswind patterns in particular, consist of four or fewer legs and the resultant linear fit extrapolation is much worse. Although there appears no direct correlation between the quality of a linear fit (for a given stepped descent) and the variation of a bulk quantity such as mean wind speed for a leg, one must question the validity of the assumption of stationarity during an entire stepped descent.

The solid lines in Fig. 8 illustrate results from using a height-based correction to the friction velocity assuming a nominally constant stress surface layer and correcting for the influence of the Coriolis force and the horizontal pressure gradient following Donelan (1990) and Banner et al. (1999). This provides an estimate of friction velocity for each flux run. It is acknowledged that such an assumption is typically only valid within the surface layer, roughly the lowest 10% of the boundary layer. However, as demonstrated in the figure, for at least seven of the nine stepped descents for which there were more than two flux runs this assumption provides an estimate that matches reasonably well with a linear fit to the stress computed at different levels over the entire stepped descent.

The above correction assumes balance between the stress, the Coriolis force and the pressure gradient. Among the assumptions made are 1) at the surface the pressure gradient is balanced by the vertical gradient of stress, 2) the stress is zero at the top of the boundary layer, 3) the wind is in geostrophic balance at the top of the boundary layer, and 4) conditions are temporally and spatially homogeneous. One expects that in hurricanes the wind at the top of the boundary layer must be consistent with gradient balance rather than geostrophic (i.e., centrifugal force must be included in the wind balance equation). Data from crosswind legs on 2 September in Hurricane Fabian support that the wind is in gradient balance even at 150 km from the storm center. Also, our data indicate that the stress does not vanish at the top of the hurricane boundary layer, but is rather approximately 1/2 to 3/4 the value at the surface. Indeed, applying corrections similar to that derived by Donelan (1990) but accounting for gradient wind and a nonzero stress at the top of the boundary layer results in a magnitude of the correction of roughly 10%–15% for most of our flux runs. This is approximately the same magnitude as simply applying the Donelan (1990) correction.

Several factors could lead to either systematic or random error in our estimate of momentum flux and ultimately the drag coefficient. In the companion paper, Drennan et al. (2007) discuss factors common to estimates for both momentum and latent heat flux including issues with sensors and methodologies. Here we focus on two issues likely to contribute most significantly to errors in our estimate of momentum flux and the drag coefficient. We estimate that the height-based correction of Donelan (1990) applied to our data provides a surface friction velocity accurate to within about 10%. We base this estimate on the range of values measured as well as the magnitude of the correction and the heights at which our measurements were obtained.

The use of the SWEMODv2 algorithm for computing the SFMR winds has a stated accuracy of 2% at 30 m s^{-1} (Uhlhorn et al. 2006, manuscript submitted to *Mon. Wea. Rev.*). A 2% uncertainty in U_{10N} would lead to approximately 4% uncertainty in the drag coefficient. Similarly, 10% uncertainty in friction velocity (as stated above) results in approximately 20% uncertainty in the drag coefficient. Taking into account these possible sources of error and those discussed in Drennan et al. (2007) we estimate an uncertainty of 30% in our measurement of drag coefficient.

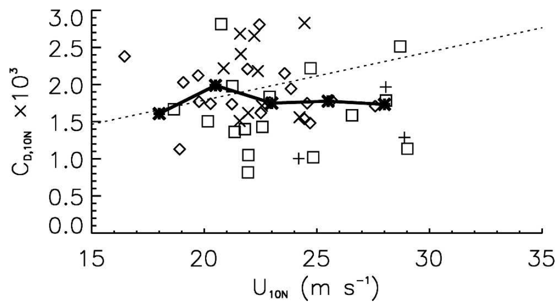

FIG. 9. Computed drag coefficient as a function of U_{10} for the 48 flux runs from this study. Data are delineated by storm (Fabian: squares and pluses; Isabel: diamonds and crosses) and by leg-wind orientation (crosswind: pluses and crosses; along-wind squares and diamonds). The thick heavy line (asterisks) represent average values for 2.5 m s^{-1} wide bins centered at 18, 20.5, 23, 25.5, and 28 m s^{-1}. The dotted line shows the fit suggested by Large and Pond (1981) extrapolated to values to 35 m s^{-1}.

4. Results and discussion

The drag coefficient provides a means to parameterize surface fluxes based on bulk measurements. Here we compute the 10-m neutral drag coefficient from our measurements of friction velocity and 10-m wind speed such that $C_{D,10N} = u_*^2/U_{10N}^2$. Figure 9 shows $C_{D,10N}$ computed from the 48 flux runs in Table 1 plotted as a function of near surface neutral wind speed, U_{10N}. At the lowest wind speeds to about 22 m s^{-1}, the drag coefficients computed in this study are nearly the same as from earlier studies (Large and Pond 1981; Smith 1980; Taylor and Yelland 2000; Fairall et al. 2003). However, at wind speeds greater than about 22 m s^{-1}, much of the data from this study fall below extrapolated results from the same earlier studies. The data points in Fig. 9 are delineated both by storm and by orientation of the flux leg to the environmental wind. Allowing for the small sample size, there is no significant difference between results when separated by leg orientation or by storm. The bold stars and line in the figure represent the bin averaged drag coefficient for 2.5 m s^{-1} wide bins centered at 18, 20.5, 23 m s^{-1}, etc. For the conditions under which these measurements were made there appears no dependence of $C_{D,10N}$ on U_{10N}.

Three of the stepped descents were completed in the right rear quadrant, one in Fabian (2 September) and two in Isabel (12 and 13 September). One stepped descent was completed in the left front quadrant (3 September in Fabian) and two were completed in the right front quadrant (4 September in Fabian and 14 September in Isabel). Because of the large amount of scatter and the relatively small number of data points it is difficult to delineate the results in any meaningful way based on the storm quadrant.

Wright et al. (2001) presented wave spectra from a Category 3 hurricane over the open ocean in 1998. Their results included individual spectra for several locations in the four storm quadrants within roughly 200 km from the storm center. Directly behind the eye, they found trimodal wave spectra that, as one moved through the right rear quadrant toward the right front, merge into one broad dominant swell propagating roughly along the wind direction. Continuing into the right front quadrant the wave spectra remain dominated by one primary swell, but oriented 30° to 60° to the right of the wind. Assuming such a pattern is typical; one may expect the stress in the right front and right rear quadrants to be diminished by the presence of following swell (cf. Drennan et al. 1999). On the other hand, stronger winds in the right front quadrant might be expected to increase the drag coefficient through wave age enhancement (i.e., younger, more strongly forced windsea waves). As indicated above, our data show no dependence when delineated by storm quadrant. However, further investigation, including acquisition of additional measurements and combining wave spectral measurements with flux measurements would allow for a test of this hypothesis.

Katsaros et al. (2002) reported on roll-type features in hurricanes observed from satellites. Such features could carry a significant portion of the momentum. Undersampling these features would lead to an under estimation of the flux and hence the drag coefficient. However, for measurements in this study there is little evidence in the aircraft data of the widespread existence of such features. A covariance summation shown in Fig. 7 from a bad run (dotted line in Fig. 7a) may suggest the existence of a coherent structure. But, this run was more the exception rather than the rule. Further, one might expect that coherent structures, depending on their alignment with the environmental wind, might lead to preferential sampling depending on the orientation of the flight leg (along wind or crosswind). Given that all of the runs used in this study passed the data quality assurance tests described in the preceding section and since we found no evidence for systematic differences between calculations from crosswind and along-wind flight legs, it is unlikely that undersampled coherent boundary layer structures contributed significantly to momentum fluxes. However, it should be pointed out that, if indeed coherent structures do exist and these structures are indeed undersampled, it is likely that they would be difficult to detect in our data. Thus further investigation into the possible existence of coherent structures is crucial for future studies.

Figure 10 shows the binned results and the associated

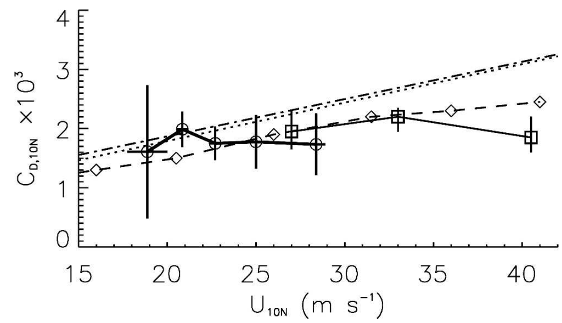

FIG. 10. As in Fig. 9 except only showing the binned values (circles) and the 95% confidence interval from this study and extrapolation of results from Large and Pond (1981) and Smith (1980), dotted and dashed–dotted, respectively. Also shown are results from Donelan et al. (2004; diamonds) and Powell et al. (2003; squares) to 42 m s^{-1}.

95% confidence interval from this study superimposed on results from earlier studies. The Large and Pond (1981) line is from eddy correlation measurements up to 20 m s^{-1} and eddy dissipation measurements to 25 m s^{-1}. The Smith (1980) line is from eddy correlation measurements to 22 m s^{-1}. Both datasets are from open-ocean long fetch conditions. In addition to our calculations at wind speeds from 20 to 30 m s^{-1}, we included the results of Powell et al. (2003) for log-profile fits for a 10–150-m surface layer and surface winds to 42 m s^{-1}. Results from Donelan et al. (2004) taken from wave-tank studies are also shown on the figure.

Results from this study are in general agreement with results from the earlier studies for wind speeds of 18 to 22 m s^{-1}. Additional comparisons at these lower wind speeds with more recent studies of the Fairall et al. (2003) COARE3.0 algorithm and Taylor and Yelland (2000) (not shown) as well show reasonable agreement, with results from COARE3.0 being slightly higher at 20 m s^{-1} than our results. However, results from the studies in wind regimes greater than 20 m s^{-1} all begin to diverge at these higher wind speeds. While Donelan et al. note a roll-off that begins around 32 m s^{-1}, it is not as pronounced as the decrease noted in the Powell et al. results (at least not for wind speeds less than 50 m s^{-1}). Our measurements suggest a roll-off at even lower wind speeds and at a smaller value of the drag coefficient. Unfortunately, data from this study were not collected at wind speeds greater than 30 m s^{-1}, and thus we cannot speculate on the behavior of the drag coefficient at these greater wind speeds.

5. Concluding remarks

In this study the first-ever direct measurements of momentum flux within a hurricane boundary layer were presented. The measurements were made from an instrumented aircraft in rain-free regions of two hurricanes. Surface values for momentum flux and 10-m drag coefficient were extrapolated from measurements made at altitudes between 70 and 383 m with near-surface wind speeds from 18 to 30 m s^{-1}.

For the lowest wind speeds in this study, up to 22 m s^{-1}, the results agree reasonably well with data from several earlier studies. For wind speeds greater than 22 m s^{-1}, calculations of drag coefficients are less than values inferred from studies conducted in wave tanks (Donelan et al. 2004) and using GPS dropsonde winds, assuming log profiles (Powell et al. 2003). This study provides substantial support to suggestions from these earlier studies that the drag coefficient does not continue to increase with wind speed, but rather levels off or even decreases. But, because of the relatively limited number of individual flux estimates (48) and the highly variable nature of the measurements, we are not able to provide a definitive description of the behavior of the drag coefficient at or approaching hurricane wind speeds. It is clear that additional measurements are needed. Further studies should attempt to obtain measurements at wind speeds ranging from 20 to 45 m s^{-1}. One of CBLAST's primary objectives was to obtain measurements in regions of surface winds approaching 50 m s^{-1}. While we were not able to accomplish that goal, it is the opinion of the authors that obtaining measurements in winds at least up to 40 m s^{-1}, and perhaps higher, is possible and a concerted effort should be placed on obtaining such measurements.

Finally, future investigations should also focus on acquiring data in all storm quadrants and coupling the results to remotely sensed sea surface conditions. Again, this was also part of the overall objectives of CBLAST, but with the limited number of storms sampled it was not fully achieved. There exists compelling evidence, at least in lighter winds, that suggest one may expect significant differences depending on storm quadrant and hence wind/wave/swell directional relationships.

Acknowledgments. This work is supported through the ONR (Grant N00014-01-F-0090) CBLAST Hurricane program and the NOAA OAR/USWRP program as well as through the NOAA/OAR laboratories AOML and ARL. We would like to acknowledge, in particular, Simon Chang and Carl Friehe (ONR) for their efforts in planning and organizing the multiyear CBLAST program, John Gaynor (OAR/USWRP) for his support, and our CBLAST co-PIs for insight into planning the experiment and interpretation of the measurements. Numerous scientists, engineers, and the flight crew at the NOAA/AOC were instrumental in obtaining this dataset: Jim Roles, Terry Lynch, Ray Tong, Barry Damiano, and others too numerous to list.

REFERENCES

Banner, M. L., W. Chen, E. J. Walsh, J. B. Jensen, S. Lee, and C. Fandry, 1999: The Southern Ocean waves experiment. Part I: Overview and mean results. *J. Phys. Oceanogr.,* **29,** 2130–2145.

Black, P. G., and Coauthors, 2007: Air–sea exchange in hurricanes: Synthesis of observations from the Coupled Boundary Layer Air–Sea Transfer Experiment. *Bull. Amer. Meteor. Soc.,* **88,** 357–374.

Brown, E. N., C. A. Friehe, and D. H. Lenschow, 1983: The use of pressure fluctuations on the nose of an aircraft for measuring air motion. *J. Climate Appl. Meteor.,* **22,** 171–180.

Crawford, T. L., and R. J. Dobosy, 1992: A sensitive fast-response probe to measure turbulence and heat flux from any airplane. *Bound.-Layer Meteor.,* **59,** 257–278.

——, ——, and E. J. Dumas, 1996: Aircraft wind measurement considering lift-induced upwash. *Bound.-Layer Meteor.,* **80,** 79–94.

DeCosmo, J., K. B. Katsaros, S. D. Smith, R. J. Anderson, W. A. Oost, K. Bumke, and H. Chadwick, 1996: Air–sea exchange of water vapor and sensible heat: The humidity exchange over the sea (HEXOS) results. *J. Geophys. Res.,* **101** (C5), 12 001–12 016.

Donelan, M. A., 1990: Air–sea interaction. *The Sea,* B. LeMehaute and D. M. Hanes, Eds., Ocean Engineering Science, Vol. 9, John Wiley and Sons, 239–292.

——, W. M. Drennan, and K. B. Katsaros, 1997: The air–sea momentum flux in conditions of wind sea and swell. *J. Phys. Oceanogr.,* **27,** 2087–2099.

——, B. K. Haus, N. Reul, W. J. Plant, M. Stiassnie, H. C. Graber, O. B. Brown, and E. S. Saltzman, 2004: On the limiting aerodynamic roughness of the ocean in very strong winds. *Geophys. Res. Lett.,* **31,** L18306, doi:10.1029/2004GL019460.

Drennan, W. M., K. K. Kahma, and M. A. Donelan, 1999: On momentum flux and velocity spectra over waves. *Bound.-Layer Meteor.,* **92,** 489–515.

——, H. C. Graber, D. Hauser, and C. Quentin, 2003: On the wave age dependence of wind stress over pure wind seas. *J. Geophys. Res.,* **108,** 8062, doi:10.1029/2000JC000715.

——, J. Zhang, J. R. French, C. McCormick, P. G. Black, 2007: Turbulent fluxes in the hurricane boundary layer. Part II: Latent heat flux. *J. Atmos. Sci.,* **64,** 1103–1115.

Emanuel, K. A., 1986: An air–sea interaction theory for tropical cyclones. Part I: Steady-state maintenance. *J. Atmos. Sci.,* **43,** 585–605.

——, 1989: The finite-amplitude nature of tropical cyclogenesis. *J. Atmos. Sci.,* **46,** 3431–3456.

——, 1995: Sensitivity of tropical cyclones to surface exchange coefficients and a revised steady-state model incorporating eye dynamics. *J. Atmos. Sci.,* **52,** 3969–3976.

Fairall, C. W., E. F. Bradley, J. E. Hare, A. A. Grachev, and J. B. Edson, 2003: Bulk parameterization of air–sea fluxes: Updates and verification for the COARE algorithm. *J. Climate,* **16,** 571–591.

Foster, R. C., 2005: Why rolls are prevalent in the hurricane boundary layer. *J. Atmos. Sci.,* **62,** 2647–2661.

French, J. R., R. Johnson, S. Beard, and T. L. Crawford, 2004:

Modification of an airborne gust probe for hurricane boundary layer research. *Proc. 26th Conf. on Hurricanes and Tropical Meteorology,* Miami, FL, Amer. Meteor. Soc., 332–333.

Friehe, C. A., and Coauthors, 1991: Air-sea fluxes and surface turbulence around a sea surface temperature front. *J. Geophys. Res.,* **96** (C5), 8593–8609.

Geernaert, G. L., K. B. Katsaros, and K. Richter, 1986: Variation of the drag coefficient and its dependence on sea state. *J. Geophys. Res.,* **91,** 7667–7679.

Hacker, J. M., and T. L. Crawford, 1999: The BAT probe: The ultimate tool to measure turbulence from any kind of aircraft (or sailplane). *J. Tech. Soaring,* **23** (2), 43–46.

Katsaros, K. B., P. W. Vachon, W. T. Liu, and P. G. Black, 2002: Microwave remote sensing of tropical cyclones from space. *J. Oceanogr.,* **58,** 137–151.

Khelif, D., S. P. Burns, and C. A. Friehe, 1999: Improved wind measurements on research aircraft. *J. Atmos. Oceanic Technol.,* **16,** 860–875.

Large, W. G., and S. Pond, 1981: Open ocean momentum flux measurements in moderate to strong winds. *J. Phys. Oceanogr.,* **11,** 324–336.

Lenschow, D. H., 1986: Aircraft measurements in the boundary layer. *Probing the Atmospheric Boundary Layer,* D. H. Lenschow, Ed., Amer. Meteor. Soc., 39–55.

Moon, I., I. Ginis, and T. Hara, 2004: Effect of surface waves on air–sea momentum exchange. Part II: Behavior of drag coefficient under tropical cyclones. *J. Atmos. Sci.,* **61,** 2334–2348.

Ooyama, K., 1969: Numerical simulation of the life cycle of tropical cyclones. *J. Atmos. Sci.,* **26,** 3–40.

Powell, M. D., P. J. Vickery, and T. A. Reinhold, 2003: Reduced drag coefficient for high wind speeds in tropical cyclones. *Nature,* **422,** 279–283.

Smith, S. D., 1980: Wind stress and heat flux over the ocean in gale force winds. *J. Phys. Oceanogr.,* **10,** 709–726.

——, and Coauthors, 1992: Sea surface wind stress and drag coefficients: The HEXOS results. *Bound.-Layer Meteor.,* **60,** 109–142.

Taylor, P. K., and M. J. Yelland, 2000: On the apparent "imbalance" term in the turbulent kinetic energy budget. *J. Atmos. Oceanic Technol.,* **17,** 82–89.

Tjernström, M., and C. A. Friehe, 1991: Analysis of a radome air-motion system on a twin-jet aircraft for boundary-layer research. *J. Atmos. Oceanic Technol.,* **8,** 19–40.

Uhlhorn, E. W., and P. G. Black, 2003: Verification of remotely sensed sea surface winds in hurricanes. *J. Atmos. Oceanic Technol.,* **20,** 99–116.

——, ——, J. L. Franklin, M. Goodberlet, J. Carswell, and A. S. Goldstein, 2007: Hurricane surface wind measurements from an operational stepped frequency microwave radiometer. *Mon. Wea. Rev.,* in press.

Wright, C. W., E. J. Walsh, D. Vandemark, W. B. Krabill, S. H. Houston, M. D. Powell, P. G. Black, and F. D. Marks, 2001: Hurricane directional wave spectrum spatial variation in the open ocean. *J. Phys. Oceanogr.,* **31,** 2472–2488.